# Supporting Information

## Microwave synchronous excitation of strong electric field and electrodeless ultraviolet radiation for effective air disinfection

Ying-Xiang Fu[1], Yu Chen[2], Yu-Qing Huang[3], Zhi-Bo Zhang[1], Yue-Hao Ma[4], Hua-Cheng Zhu (✉)[3], Ye Du (✉)[1]

1 College of Architecture and Environment, Sichuan University, Chengdu 610000, China

2 New Energy Research Institute, School of Environment and Energy, South China University of Technology, Guangzhou Higher Education Mega Centre, Guangzhou 510006, China

3 College of Electronic and Information Engineering, Sichuan University, Chengdu 610065, China

4 Sichuan University−Pittsburgh Institute, Sichuan University, Chengdu 610065, China

Number of pages:32

Number of figures: 7

Number of tables: 2

### Text S1 Chemicals and Reagents

Using potassium iodide (KI, analytical reagent, Kelong Chemical Co., LTD., Chengdu, China), sodium tetraborate decahydrate ($Na_2B_4O_7 \cdot 10H_2O$, analytical reagent, Shanghai Macklin Biochemical Co., LTD., Shanghai, China), and potassium iodate ($KIO_3$, analytical reagent, Shanghai Macklin Biochemical Co., Ltd) were used to prepare KI/ $KIO_3$ actinometer stock solution.

✉ Corresponding authors
E-mail: hczhu@scu.edu.cn (H. Zhu); duyeah@scu.edu.cn (Y. Du)

The *Escherichia coli* strain was purchased from Qingdao Biotechnology Co., Ltd. in Beijing, China. *Bacillus subtilis* (*B.* subtilis) strains were purchased from the General Microbial Culture and Collection Center of China (Beijing). Luria-Bertani broth and Luria-Bertani nutrient AGAR were purchased from Beijing Aobo Xing Biotechnology Co., LTD. (Beijing). *Escherichia coli* in actual wastewater was detected using sodium carmine basic sulfite AGAR from Qingdao Hope Biotechnology Co., LTD.

Sodium chloride (NaCl, analytical reagent, Cologne Chemical Co., LTD.) was dissolved in ultrapure water to prepare physiological saline with a concentration of 0.9%. Phosphate buffered saline purchased from Shanghai Zhong Qiao Xin Zhou Biotechnology Co., LTD. (Shanghai, China). 5, 5-dimethyl-1-pyridine oxide (DMPO),2, 2,6, 6-tetramethylpiperidine (TMP), tert-butanol and L-histidine were purchased from Aladdin Chemical Company in Shanghai, China. Live/dead BBcellProbe N01/ PI bacterial viability kits were purchased from BestBio (Shanghai, China).

**Text S2 *E. coli* and *B. subtilis* preparation and counting**

*Escherichia coli (E. coli)* and *Bacillus subtilis (B. subtilis*) strains were stored in glycerol stock solution at -80 °C. Frozen *E. coli or B. subtilis* cultures thawed in water at 37 °C under aseptic conditions. Transfer 50 μL of the bacterial suspension to 200 mL of autoclaved LB nutrient solution using a pipette. Then shake and incubate at 160 r/min, 37 °C. Incubate *E. coli* for 18 hours and *B. subtilis* for 48 hours. After

incubation, centrifuge the culture medium at 4800 r/min for 5 minutes. Discard the supernatant and resuspend the microspheres in a specified volume of sterile physiological saline and mix well. Repeat this process twice. Resuspend the precipitate in brine and analyze the resulting mixture using a UV spectrophotometer (INESA, China). Dilute the mixture to an initial cell concentration of approximately $10^6$ to $10^8$ CFU /mL.

The bacteria were quantified using dilution plating (Pezeshkpour et al., 2018). 50 μL of the appropriately diluted water sample was evenly spread over the surface of the LB AGAR plate using a sterile L-shaped spreader. Each dilution gradient includes three repeat samples. Incubate the petri dishes upside down at 37 °C for 24 hours. Select plates containing 30 to 300 colonies for counting and calculate the average colony count.

**Text S3 Microwave-excited strong electric field combined with ultraviolet disinfection device**

High-concentration bacterial suspensions were atomized into microbial aerosols and introduced as solutes into the gas-phase dispersion system. In a Y-shaped three-way quartz tube, they were turbulently mixed with filtered clean air to form a continuous flow aerosol with adjustable concentration gradients. The flow channel structure was optimized through fluid mechanics estimation to ensure that the average residence time of aerosol particles in the reaction chamber was 0.5 to 0.8 seconds at the set flow rate. This duration was calculated based on the inactivation kinetics

model of the target microorganisms to ensure sufficient exposure of the microorganisms to the subsequent coupled disinfection field. The treated aerosols were captured by a sampler at the end of the chamber to obtain viable bacteria, forming a complete experimental loop.

The main body of the disinfection chamber is made of stainless steel with dimensions of 300 mm × 200 mm × 150 mm, ensuring structural strength and corrosion resistance. The aerosol transmission channel is made of quartz tube, a choice based on its unique material advantages in a multi-physical field coupling environment. At the 2.45 GHz microwave band, the quartz tube demonstrates excellent microwave transmission performance due to its low loss characteristics, with a microwave absorption rate through the tube wall of less than 0.1% and an insertion loss of only 0.15 to 0.3 dB, and the attenuation of the cavity electric field does not exceed 2.3%. In the 254 nm ultraviolet radiation band, the transmission rate of the quartz tube exceeds 90%, and after 1000 hours of continuous irradiation, the attenuation is less than 3%, ensuring efficient transmission and long-term stability in the main sterilization band. In the presence of an electric field, the quartz tube, with a volume resistivity of $10^{16}$ Ω·cm, avoids conductive interference and generates only 0.7% dielectric polarization loss in an alternating electric field of 3.5 kV/cm. The combined characteristics of low loss, high transmission, and high insulation make the quartz tube an ideal transmission medium for the microwave-ultraviolet collaborative system.

The microwave system adopts a 2.45 GHz solid-state microwave source, with an

output power that can be continuously adjusted within the range of 0 to 200 W to meet different processing requirements. The system is equipped with a double-ridged waveguide with low loss characteristics, and the voltage standing wave ratio (VSWR) is controlled within 1.5 to ensure efficient transmission of microwave energy to the disinfection chamber. The structural parameters of this double-ridged waveguide were optimized through COMSOL multiphysics simulation and experimental verification, and were determined to be: wide side 35 mm, narrow side 20 mm, ridge spacing 4 mm, and ridge width 6 mm. When air is used as the medium, the local electric field intensity generated by this structure can reach $3.083\times10^5$ V/m, which is 13.3 times higher than that of the traditional WR430 waveguide, and the microwave power absorption conversion efficiency is increased by 180 times. Through system experimental research, a quantitative correspondence relationship between the input microwave power and the electric field intensity inside the waveguide was established: when the input power increases from 50 W to 200 W, the electric field intensity correspondingly increases from 136 kV/m to 273 kV/m. This precise correspondence relationship provides an important basis for the subsequent energy efficiency optimization of the disinfection system.

The ultraviolet system employs microwave-excited argon-mercury electrodeless ultraviolet lamps with a coaxial structure designed to have an inner diameter of 3 mm and an outer diameter of 7 mm, and is equipped with a 5 mm igniter. This structure enhances the local electric field to $3.6\times10^4$ V/m, which is three times the applied electric field, thereby reducing the breakdown power of the argon-mercury mixed

electrodeless lamp to 50 W and achieving an energy conversion efficiency of over 90%. The main peaks of ultraviolet radiation are at 365 nm and 253 nm, with 253 nm being the main band for sterilization. At an input power of 50 W, the coefficient of variation (COV) of axial light intensity uniformity is 0.15, and the average ultraviolet intensity at 10 cm from the lamp surface is 0.8 to 1.6 mW/cm$^2$. To ensure stable operation, the lamps are axially fixed and installed with a spacing of less than 500 mm, and the working surface temperature is controlled below 300 °C. This design offers excellent durability, with a radiation intensity decay of less than 5% within the first 100 hours, an expected service life of over 20,000 hours, and the ability to withstand more than 10,000 switch cycles.

After system integration, the aerosol flow rate was designed to be adjustable within the range of 50 to 200 mL/min, forming a multi-parameter coordinated control system with microwave power and ultraviolet intensity. Microorganisms in the disinfection chamber are simultaneously exposed to the coupling effect of the strong electromagnetic field generated by the double-ridge waveguide and the ultraviolet radiation produced by the electrodeless lamp, achieving efficient inactivation. The detailed simulation calculation of the ultraviolet subsystem is presented in Text S9, and the optimization design calculation of the waveguide structure is provided in Text S10.

**Text S4 Response surface analysis**

This study employed a three-factor, three-level Box-Behnken experimental

design, and utilized the Design-Expert software to generate 17 experimental schemes including the central point. The three independent variables were ultraviolet dose (UV), pulsed electric field power ($P_{EF}$), and aerosol flow rate (Q), each factor was encoded at three levels: -1, 0, and +1. The dependent variable was the logarithm of the microbial inactivation rate, denoted as Y.

Based on the experimental data, a second-order polynomial response surface model is constructed, and its standard form is:

$$Y = \beta_0 + \sum_{i=1}^{3} \beta_i X_i + \sum_{i=1}^{3} \beta_{ii} X_i^2 + \sum_{i<j}^{3} \beta_{ij} X_i X_j + \varepsilon$$

Here, $\beta_0$ is the constant term, $\beta_i$ is the linear coefficient, $\beta_{ii}$ is the quadratic term coefficient, $\beta_{ij}$ is the interaction term coefficient, $x_i$ and $x_j$ are the encoded independent variables, and ε is the residual term.

The results of the analysis of variance indicated that the p-value of the overall significance test of the model was less than 0.01, suggesting that the regression equation was statistically significant; the p-value of the lack-of-fit test was greater than 0.05, indicating that the model did not omit key variables and was well-fitted; the p-values of the Shapiro-Wilk test and the Breusch-Pagan test were both greater than 0.05, confirming that the residuals followed a normal distribution and had homoscedasticity. Cross-validation showed that the predicted determination coefficient Rpred2 was greater than 0.9 and $Q^2$ was greater than 0.8, indicating that the model had good generalization ability and prediction accuracy.

The validated model was used to draw three-dimensional response surface plots and contour plots to visually demonstrate the influence laws of each factor and their

interaction on the inactivation effect. The synergy effect of microwave power and ultraviolet intensity was particularly examined: when the two factors were at high-level combinations, the response surface showed a significant synergistic enhancement feature, and the inactivation rate increased steeply with the increase in dose; while in the low-level region, the surface slope was gentle, indicating a clear interaction threshold effect. The non-parallel distribution of the contour lines further confirmed the significant interaction between the two physical fields.

The optimal process parameter combination was determined by solving the extremum points of the regression equation. Within the experimental design range, the best conditions corresponding to the maximum inactivation rate predicted by the model were: ultraviolet dose X mJ/cm², electric field intensity Y kV/m, and aerosol flow rate Z mL/min, with a predicted response value of Y_pred. To verify the prediction reliability of the model, three parallel validation experiments were conducted under these conditions, and the average measured value was Y_obs. The relative error between the predicted value and the measured value was δ%, which was within the acceptable range, indicating that the response surface model could accurately predict the process performance of the microwave-ultraviolet synergistic disinfection system.

**Text S5 Preparation of High Salinity Medium**

Preparation and optimization of high salinity medium: To construct a stable and controllable high-salt stress environment, NaCl was added in a gradient of 1.0 mol/L,

1.5 mol/L, and 2.0 mol/L to the basal LB medium. The conditions with 1.5 mol/L NaCl were screened out through pre-experiments as the stress threshold conditions. At this concentration, the bacterial growth inhibition rate was greater than 80% and it was not completely lethal. The pH of the medium was maintained at around 7.0 by adding 20 mmol/L of HEPES buffer to avoid the interference of pH fluctuations caused by high salt ion strength on the experimental results. After preparation, autoclave at 121 °C for 20 minutes, aliquot into sterile petri dishes, 15 mL per dish, and store in the dark at 4 °C for future use.

**Text S6 Photoreactivation analysis method**

Characterization of the disinfection process using the Chick-Watson first-order dynamics model (Hijnen et al., 2006). Disinfection performance was evaluated using inactivation rate constants and bacterial inactivation efficiency. The formula is described as follows:

$$\text{Inactivation rate}=\log(N_0/N) = K_d \times D \quad \text{(S1)}$$

Where $K_d$ is the inactivation rate constant ($cm^2/mJ$) and D is the UV dose ($mJ/cm^2$).

The photoactivation properties of *E.coli* were evaluated using photoactivation rate and photoactivation models. The maximum reactivation value was the bacterial count (CFU/mL) of *E.coli* after complete photoactivation. The formula for calculating the photoreactivation rate is as follows (Lindenauer and Darby, 1994):

$$\text{photoreactivation rate} = (N_t - N)/(N_0 - N) \times 100\% \quad \text{(S2)}$$

Here, $N_0$ represents the initial bacterial count before disinfection (CFU/mL), N represents the bacterial count after ultraviolet irradiation (CFU/mL), and $N_t$ represents the bacterial count after photoactivation (CFU/mL).

The photoreactivation process of microorganisms can be described by survival rate, which is independent of the initial bacterial count. The survival rate (S) is calculated as follows (Kashimada et al., 1996):

$$S = N_t/N_0 \times 100\% \quad \text{(S3)}$$

The photoreactivation process of microorganisms can be modeled using logistic regression equations as follows (Nebot Sanz et al., 2007):

$$S = S_m/\left[1+(S_m/S_0 - 1)\times e^{-k_2 \cdot S_m \cdot t}\right] \quad \text{(S4)}$$

Where Sm represents the maximum survival rate (%), $S_0$ represents the survival rate after disinfection (%), and $k_2$ represents the secondary reactivation rate constant ($\%^{-1}h^{-}$).

The model parameters in this model are used to predict the results of the experiment, not to represent the actual reactivation rate constant. The formula for recalculating the light reactivation rate constant is as follows (Li et al., 2017):

$$K = ds/dt = k_2(S_m - S)S \quad (S5)$$

The maximum reactivation rate constant $K_{max}$ is determined as follows: The reactivation rate K peaks when the survival rate reaches 50% of the maximum survival rate.

$$K_{max} = k_2 S_m^2/4 \quad (S6)$$

In this study, a logistic regression model was used to fit the photoreactivation process. The model parameter $k_2$ was estimated and compared with $k_{max}$, where$_m$ S represents the maximum survival rate of the bacteria after reactivation, the degree of light reactivation, and k represents the maximum reactivation rate of the bacteria.

**Text S7 Multiphysics Coupling Simulation Experiment**

This study aims to establish a multi-physics coupling model of the single-cell-electrode system and quantitatively analyze the electroporation dynamics of the cell membrane under the action of nanosecond pulsed electric fields. The simulation is based on the COMSOL Multiphysics platform, and by solving the coupled system of Maxwell's equations and electroporation dynamics equations, key parameters such as transmembrane potential, pore density evolution, and membrane conductivity changes under the pulse action are obtained, providing a theoretical basis for subsequent experimental design (Guo et al., 2022).

Considering the balance between computational efficiency and accuracy, the simulation adopts a two-dimensional axisymmetric geometry to describe the single-

cell-electrode system. The coordinate origin is set at the center of the cell, with the Z-axis as the symmetry axis and the radial coordinate as r. The geometric model consists of three concentric regions: the intracellular domain, the cell membrane, and the extracellular domain. During modeling, basic shapes such as circles and rectangles are inserted in sequence in the COMSOL geometry nodes, and the overall assembly is completed through Boolean merge operations; subsequently, the explicit selection function is used to assign independent labels to the cell membrane, intracellular/extracellular domains, and electrode boundaries for subsequent material property assignment and boundary condition application (Guo et al., 2026).

The dielectric properties of the cell membrane are described using the multi-pole Debye model to accurately characterize its dispersion behavior in the nanosecond pulse frequency band. The relationship between the relative permittivity and frequency is:

$$\varepsilon_r(f)=\varepsilon_\infty+\sum_{m=1}^{N}\frac{\Delta\varepsilon_m}{1+j2\pi f\tau_{vm}} \quad (S7)$$

Here, εr(f) is the frequency-dependent relative permittivity, ε∞ is the high-frequency limit relative permittivity, Δεm is the contribution of the mth polarizability to the relative permittivity, τm is the corresponding relaxation time, and N is the total number of polarizabilities. The cytoplasm and extracellular fluid are also treated as dispersive media, with the number of polarizabilities and relaxation times taken from typical values reported in the literature. The cell membrane is set as a dispersive medium, and the conductivities and dielectric parameters of the cytoplasm and extracellular fluid are determined based on the most commonly used typical values in

the literature to ensure the universality and scalability of the model (Wang et al., 2019).

The physical field configuration activates the current module to solve the global electromagnetic field distribution. The membrane surface pore density variable N (unit: $m^{-2}$) is defined in the boundary ordinary differential equation and differential algebraic equation nodes, and the electroporation kinetics model is established. The electroporation process involves the generation and evolution of hydrophilic micropores in the lipid bilayer, and the pore density N changes with time and transmembrane potential according to:

$$\frac{dN}{dt} = \alpha \cdot e^{\left(\frac{V_m}{V_{ep}}\right)^2} \cdot \left(1 - \frac{N}{N_0} \cdot e^{-q\left(\frac{V_m}{V_{ep}}\right)^2}\right) \quad \text{(S8)}$$

In the formula, α represents the nucleation rate coefficient, Vep is the characteristic electroporation voltage, N0 is the saturated pore density, and q is a parameter related to the energy barrier. The evolution of membrane conductivity with pore density is determined by the time-varying conductivity formula:

$$\sigma_m(t) = +N(t,(t))\pi K \sigma_{m0} V_m \sigma_p r_p^2 \quad \text{(S9)}$$

Here, σm0 represents the static baseline membrane conductivity, σp the pore conductivity, rp the pore radius, and K a coefficient proportional to the pore entrance length and energy barrier, with its expression given as:

$$K = (e^{v_m} - 1) / \left[\frac{(\omega_0 e^{\omega_0 - nv_m} - nv_m) e^{v_m}}{\omega_0 - nv_m} - \frac{(\omega_0 e^{\omega_0 + nv_m} + nv_m) e^{v_m}}{\omega_0 + nv_m}\right] \quad \text{(S10)}$$

In the formula, vm = VmF/RT, where F is the Faraday constant, R is the gas constant, T is the absolute temperature, and ω0 and nvm are parameters related to the membrane potential and the energy density of the micropores.

The transmembrane potential is obtained by solving the electromagnetic control equation. The potential φ at any point inside the cell satisfies:

$$-\nabla\cdot\left(\varepsilon_0\varepsilon_i\frac{\partial\nabla\varphi}{\partial t}\right)-\nabla\cdot\left(\sigma_i\nabla_\varphi\right)=0 \quad \text{(S11)}$$

Here, ∇ represents the gradient operator, ε0 = 8.85×10−12 F/m is the vacuum permittivity, and εi and σi are the relative permittivity and conductivity of each component, respectively. The transmembrane potential is defined as the difference in potential between the outside and inside of the cell membrane:

$$V_m(t)=\varphi_0(t)-\varphi_i(t) \quad \text{(S12)}$$

The resting potential of cells is approximately tens of millivolts, which has a negligible impact on the calculation of transmembrane potential and pore density, and thus is ignored in the simulation. To address the issue of non-shared grids on both sides of the cell membrane due to its extremely thin thickness, a non-local coupling operator is introduced to establish the in→out and out→in mappings. The mapping rule adopts a generalized squeeze transformation, which establishes a one-to-one correspondence between the source and target boundaries through radial-axial coordinate transformation, thereby achieving an accurate calculation of the transmembrane potential difference. The grid division strategy is shown in Figure S3, with local refinement in the cell membrane area to capture the rapidly changing field gradient.

The solution process is divided into two stages: Firstly, a frequency-domain analysis is conducted to verify the correctness of the dispersion model; then, the steady-state solution of the initial field distribution is obtained as the initial condition

for the time-domain solution. The time-domain solution adopts an adaptive time step algorithm to accurately capture the rapid dynamic process of the rising edge of the nanosecond pulse. After the calculation is completed, the results such as the potential distribution, the transmembrane voltage time course, the evolution of pore density, and the membrane conductivity distribution are extracted and compared with the subsequent experimental measurements for verification.

**Text S8 *E. coli* electroporation model correction method**

When creating a three-dimensional model to simulate the electroporation effect of Escherichia coli with a "capsule" geometry (consisting of two semi-circular arcs and a straight line segment in the middle). The core challenge of this model,compared with the standard spherical model available on the comsol website, lies in its composite geometric properties. The model encounters a fundamental solution paradox after introducing dynamic conductivity, which varies in real time according to pore density and transmembrane voltage at the boundary: Solver dependency "dead loop" : The solver needs to know the conductivity of the Domain to calculate the potential distribution, but the calculation of conductivity depends on the pore density (N) and transmembrane voltage ($V_m$) that can only be calculated at the Boundary. The calculation of these variables at the boundary, in turn, requires knowledge of the potential distribution of the domain. This dead loop causes the model to oscillate back and forth between "undefined variable" and "no source point found," failing to converge. Since a single tool cannot handle both arcs and straight lines at the same

time, we have to create dedicated tools (stretching operators) for each of them and create variables that can intelligently invoke these tools based on position. The entire correction process is divided into three key levels: the stretching operator (ground), transmembrane voltage (first layer), and dynamic conductivity (top layer).

The spherical model on the official website only requires two operators, while our capsule model needs eight. sqrt($x^2+y^2$)Create four operators for the arc part: mem_in_to_out, mem_out_to_in, wall_in_to_out, wall_out_to_in. Using the radial projection formula based on, project a point precisely from an arc to another concentric arc. Create four operators for the straight line part: membrane_in_to_out_straight, membrane_out_to_in_straight, wall_in_to_out_straight, wall_in_to_out_straight. Using the logic of absolute coordinate positioning is the key to ensuring a successful mapping of the straight line part.

$V_m$ It is a variable defined on the boundary, and its calculation requires obtaining the potential value from the outer boundary. $V_{m\_wall}$ Use the if statement as an example: if(abs(y)>y_wall_junc,wall_out_to_in(V),wall_out_to_in_straight(V)-V)

y_wall_junc is the y-coordinate of the junction point of the cell wall arc and the straight line as defined in the parameter. $V_m$ When a point is on the arc (abs(y)>y_wall_junc) it calls the arc operator wall_out_to_in; When the point is on a straight line, it calls the line operator wall_out_to_in_straight. This correction allows for the automatic invocation of the corresponding correct stretching operator based on one's position during the calculation.

The final step to solve the infinite loop requires defining a series of variables in the domain (e.g.$V_{m\_wall}$,sigma_wall_t), and the calculation of these variables depends on the variables on the boundary (e.g.$V_{m\_wall,}$ $N_{wall}$) Use the if statement again to apply the logic from Part 2 to all the variables that need to be defined in the field.

$V_{m\_wall}$ Definition of dimensionless voltage:

if(abs(y)>y_wall_junc,wall_in_to_out($V_{m\_wall}$),wall_in_to_out_straight($V_{m\_wall}$))*F_const_/(R_const_*T_abs)

The wall_in_to_out series of operators is used here because values on the inner boundary need to be propagated over the entire domain. $V_{m\_wall}$ The If statement ensures that the corresponding operator is correctly invoked in both arc and straight line areas.

The definition of sigma_wall_t for the dynamic part of conductivity: $V_{m\_wall}$

if(abs(y)>y_wall_junc,wall_in_to_out(N_wall),wall_in_to_out_straight(N_wall))*sigma_p*pi*rp^2*k_wall is exactly the same, Here the if statement is used to intelligently invoke wall_in_to_out or wall_out_to_in_straight, thus safely and correctly introducing the hole density N_wall on the boundary into the domain calculation.

**Text S9 Microwaves light up the electrodeless ultraviolet lamp to excite ultraviolet light**

When the 2.45GHz microwave passes through the waveguide system to the quartz lamp tube filled with argon-mercury mixture, the alternating electromagnetic

field ionizes the gas inside the tube.

The acceleration effect of the microwave electric field on free electrons can be described by the Lorentz force equation:

$$F=q\cdot(E+v\cdot B) \tag{S13}$$

Here q is the amount of charge carried by the electron, and v is the speed at which the electron moves.

In the microwave band of 2.45 GHz, the kinetic energy gained by the electron in the alternating electric field is sufficient to overcome the ionization energy of argon to form the initial plasma:

$$E_k=\frac{1}{2}m_e v^2>15.75eV \tag{S14}$$

The process follows a stepwise ionization mechanism:$Hg^*\rightarrow Hg+h\nu(253.7nm)$

At the beginning, argon is ionized first to form a plasma carrier:$Ar+e^-\rightarrow Ar^++2e^-$

Subsequently, the excited argon atoms transfer energy to the mercury atoms through collisions:

$$Ar^*+Hg\rightarrow Ar+Hg^*$$

As a result, the mercury atom in the excited $6^3P_1$ orbital emits ultraviolet light at 253.7 nm when it transitions to the ground state:

$$Hg^*\rightarrow Hg+h\nu(253.7nm)$$

Finally, the microwave power density maintains plasma stability through the electron cyclotron resonance effect, and the equations designed are as follows:

$$\omega_{ce}=\frac{eB}{m_e}\approx 2.45GHz \tag{S15}$$

Here is the electron cyclotron frequency. $\omega_{ce}$ Resonance absorption occurs when

electrons match microwave frequencies, significantly enhancing energy coupling efficiency.

The device achieves efficient excitation of ultraviolet radiation by microwaves through precise electromagnetic field design and plasma parameter control, providing an optimal physical field environment for aerosol disinfection. In this study, COMSOL software was used to model the multi-physics field coupling of the compact coaxial microwave plasma electrodeless ultraviolet lamp. The modeling process mainly involved coupling analysis of the two physical fields of electromagnetic field and plasma, coaxial line design, geometric modeling, etc.

(1) Equations for multi-physics coupling:$\omega_p=\sqrt{\frac{n_e q^2}{m_e \varepsilon_0}}$

Electromagnetic field for simulating microwave propagation by solving the Helmholtz equation:

$$\nabla\times\mu^{-1}\nabla\times\vec{E} = (\omega^2\varepsilon_0\varepsilon_r\text{-}j\omega\sigma)\vec{E} \tag{S16}$$

Where is the microwave electric field intensity; $\vec{E}$ $\omega$ For microwave angular frequency, 2.45 GHz; $\varepsilon_0$ For vacuum dielectric constant; $\varepsilon_r$ For the relative dielectric constant of the material, 4.2 for the quartz tube and 1 for the plasma region.

The plasma model uses the Drude model, treating the plasma as the equivalent dielectric material:

$$\varepsilon_{rp}=1\text{-}\frac{\omega_p^2}{\omega^2+v_m^2}\text{-}j\frac{\omega_p^2 v_m}{\omega(\omega^2+v_m^2)} \tag{S17}$$

$$\omega_p=\sqrt{\frac{n_e q^2}{m_e \varepsilon_0}} \tag{S18}$$

Where $\omega_p$ is the frequency of the plasma; $v_m$ Is the frequency of electron collisions, taken as $1\times10^{10}$ Hz; $n_e$ For electron density, generally take $1\times10^{20}$ m

(2) Impedance matching formula for coaxial design:

$$Z_0=\frac{60}{\sqrt{\varepsilon_r}}\times \ln\frac{b}{a}=50\Omega \quad \text{(S19)}$$

Among them, *a* is the radius of the inner conductor; *b* is the radius of the outer conductor.

(3) Homogeneity evaluation formula:

$$COV=\frac{\sqrt{\frac{\sum n(I_i-\bar{I})^2}{n}}}{\bar{I}} \quad \text{(S20)}$$

Here is the $I_i$ *i-th* sampling point; $\bar{I}$ Is the average light intensity.

(4) Geometric modeling and parametric design:

The design of the coaxial structure is as follows: a hollow inner conductor of diameter 2a with a built-in vacuum quartz tube, an outer conductor of diameter 2b with an electrically shielded Faraday cage, and an igniter designed as a metal rod of length 5 m connected to the tip of the inner conductor. The parameters involved are as follows: the microwave frequency is set to 2.45Hz, the boundary conditions are set as ideal conductors, and the material parameters are selected from COMSOL's material library.

**Text S10 Microwave excites a strong electric field in a double-ridge waveguide**

The double-ridge waveguide used in this study is a key component of the microwave transmission system and is designed based on improvements to the WR284 standard waveguide. The mechanism by which microwaves form strong electric fields in the double-ridge waveguide is mainly reflected in the following three aspects: First, in terms of microwave transmission, the microwave energy generated

by the solid-state microwave source is transmitted to the double-ridge waveguide converter through the impedance matched coaxial cable, and the $TE_{10}$ mode excitation ensures efficient coupling of microwaves. Secondly, in terms of the electric field enhancement mechanism, the special design of the double ridge structure produces a significant field strength aggregation effect. The electric field line density in the narrow area between the ridges at intervals of 5 to 10 mm can reach 3 to 5 times that of ordinary waveguides. Meanwhile, the ridge structure optimizes the waveguide characteristic impedance to around 50 Ω, achieving a good matching characteristic with a voltage standing wave ratio VSWR not greater than 1.5.

Finally, in terms of the field strength distribution, the system can generate a strong electric field of 100 to 200 kV/m at an input power of 50 W, and its centrally symmetrical field strength distribution pattern makes the uniform area account for more than 80%, combined with an energy conversion efficiency of over 90% and a heat loss characteristic of less than 5%, This makes the structure particularly suitable for applications that require high field strength and high efficiency, such as air disinfection. This structure-optimized electric field enhancement scheme achieves efficient localized concentration of energy by precisely controlling the spatial distribution of the electromagnetic field.

The strong electric field of the device is mainly formed by the combined action of the Double-Ridge Waveguide and the Microwave Cavity, which can be theoretically decomposed as:

Solve for the electric field distribution within the waveguide. The $TE_{10}$ mode

reveals that in a rectangular waveguide, the distribution of the electric field intensity can be derived from the wave equation: $\vec{E}$

$$\nabla^2\vec{E}+k_c^2\vec{E}=0 \tag{S21}$$

Among them

$$k_c=\sqrt{\left(\frac{m\pi}{a}\right)^2+\left(\frac{n\pi}{b}\right)^2} \tag{S22}$$

For the cutoff wavenumber, *m* and *n* are mode exponents, where *m=1 and n*=0 in $TE_{10}$ mode.

The field enhancement effect of the double-ridge waveguide can be approximated as:

$$E_{max}=E_0\cdot\frac{a}{a'}\cdot\frac{b}{b'} \tag{S23}$$

Where *a* and *b represent* the normal waveguide size and represent the equivalent size of the ridge waveguide after reduction. $a'$ $b'$ Because the ridge structure reduces the effective size of the waveguide, the electric field strength can be increased by 3 to 5 times. $E_{max}$ The mode of the ridge waveguide is basically the same as that of the rectangular waveguide, with the fundamental mode being $TE_{10}$ mode.

The cut-off wavelength of the $TE_{10}$ mode is calculated using the transverse resonance method, and the simplified formula of the waveguide mode in this experiment is for the $TE_{10}$ mode:

$$\lambda_c=2(a-c)\sqrt{1+\frac{2.45+0.2c}{a(b-c)}\ln\csc\left(\frac{\pi d}{2b}\right)} \tag{S24}$$

The formula applies under the condition that $0.01 \le d/b \le 1, 0 \le c/a \le 0.45$. The fundamental mode cut-off frequency is calculated to be 2.04 GHz and the fundamental mode cut-off wavelength is 0.147 m.

Electric field intensity regulation method:

（1） Directly adjusting the output power of the solid-state microwave source:

$$E_{peak} \propto P \tag{S25}$$

(2) Alter the resonator tuning, that is, change the $Q$ value, adjust the cavity size, or load the medium to optimize the $Q$ value for enhanced electric field focusing.

(3) Waveguide ridge spacing adjustment, mechanically adjusting the double ridge spacing, reducing the double ridge spacing can enhance the local electric field intensity. $a'$

$$E_{max} \propto \frac{1}{a'} \tag{S26}$$

(4) Aerosol dielectric constant matching, optimizing aerosol flow rate or humidity to match the dielectric constant and reduce energy reflection (VSWR optimization). $\varepsilon_r$

Multiphysical field control equations:

(1) Electromagnetic field part:

Determining the distribution of the electric field by solving Maxwell's equations and Helmholtz equations:

$$\nabla \times \mu^{-1} \nabla \times \vec{E} = k_0^2 \left( \varepsilon_r - j \frac{\sigma}{\omega \varepsilon_0} \right) E \tag{S27}$$

Here, $k_0$ represents the wavenumber of free space and is the electrical conductivity $\sigma$

(2) Thermal field part:

Substitute the power density absorbed by the quartz material into the heat conduction equation to calculate the temperature distribution:

$$\rho_m C_p \frac{\partial T}{\partial t} - k_m \nabla^2 T = \pi f \varepsilon_0 \varepsilon |E|^2 \quad \text{(S28)}$$

Where is the density of the material, is the specific heat capacity of the material, and $\rho_m$ $C_p$ $k_m$ is the thermal conductivity of the material.

Geometric model construction:

Symmetrical double-ridge waveguides and fine quartz hollow tubes with a diameter of 2 mm placed along the Z-axis at the center of the ridge.

Boundary conditions and parameter Settings:

(1) Electromagnetic boundary: The waveguide surface is a perfect electrical conductor, and the excitation port is set to a wave port perpendicular to the electric field.

(2) Thermal boundary: Consider forced convection of air flow in the quartz tube to eliminate the interference of microwave-generated thermal effects on bacterial inactivation:

$$k_n \frac{\partial T}{\partial n} = \mathrm{h}(T_{air} - T) \quad \text{(S29)}$$

Where $h$ is the heat transfer coefficient.

(3) Material parameters: Parameters from the COMSOL material library.

(4) Microwave frequency: 2.45GHz.

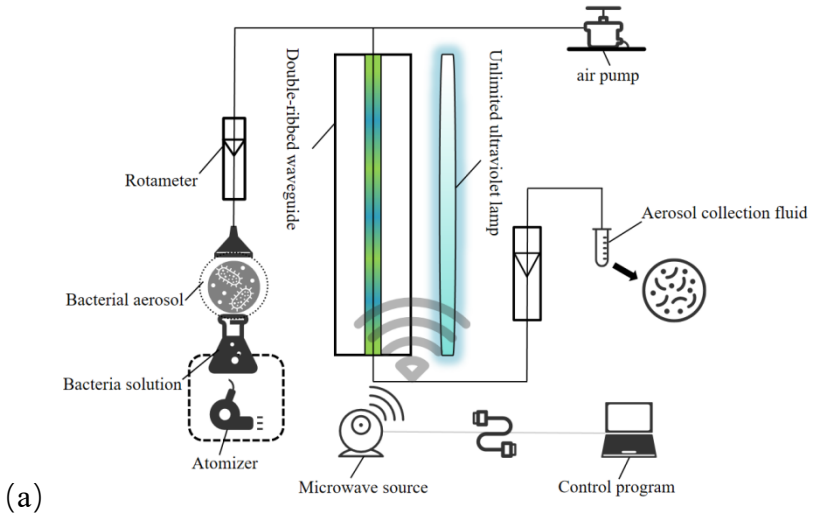


(a)

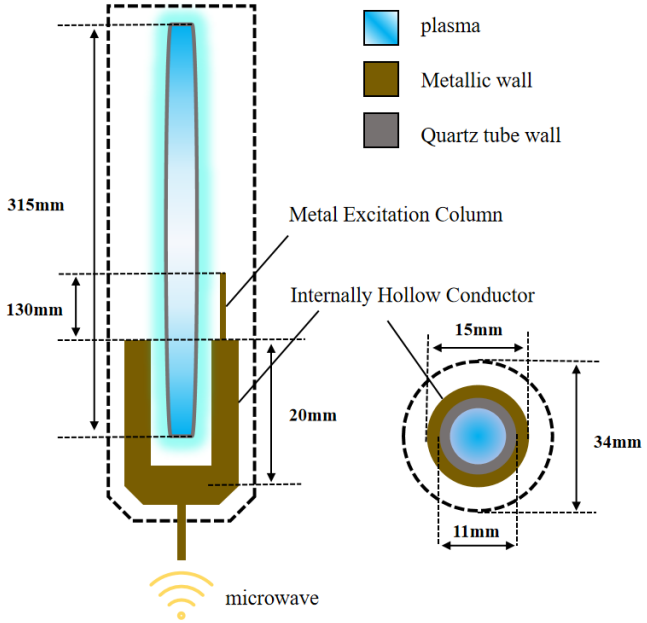


(b)

**Figure S1 Schematic diagram of the experimental setup:** (a) Schematic diagram of the core disinfection reaction chamber setup; (b) Coaxial structure of the ultraviolet lamp and schematic diagram of microwave-lit electrodeless ultraviolet lamp.

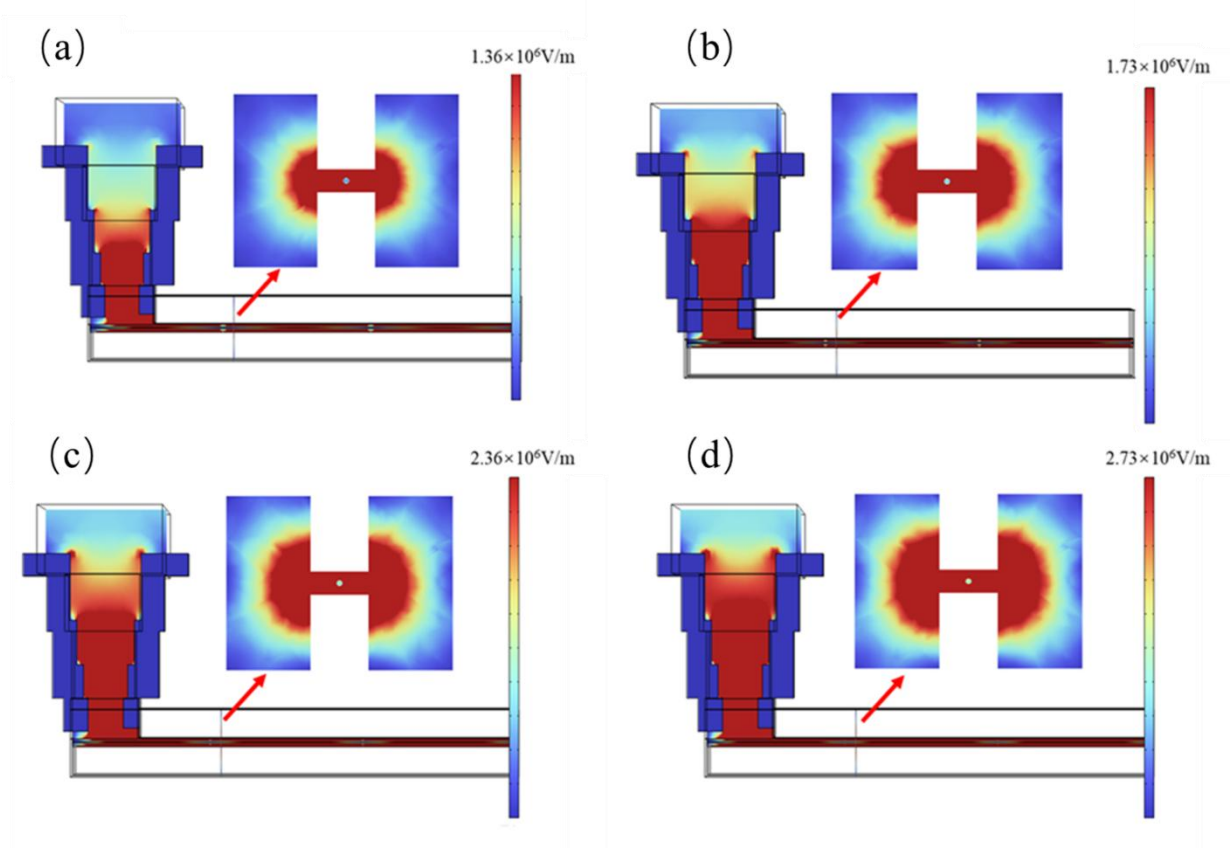


1

**Figure S2 Correspondence of electric field and input microwave power in a double-ridge waveguide:** (a) Cloud map of electric field distribution in the ridge waveguide at 50 W input power; (b) Cloud map of electric field distribution in the ridge waveguide at 100 W input power; (c) Cloud map of electric field distribution in the ridge waveguide at 150 W input power; (d) Cloud map of electric field distribution in the ridge waveguide at 200 W input power.

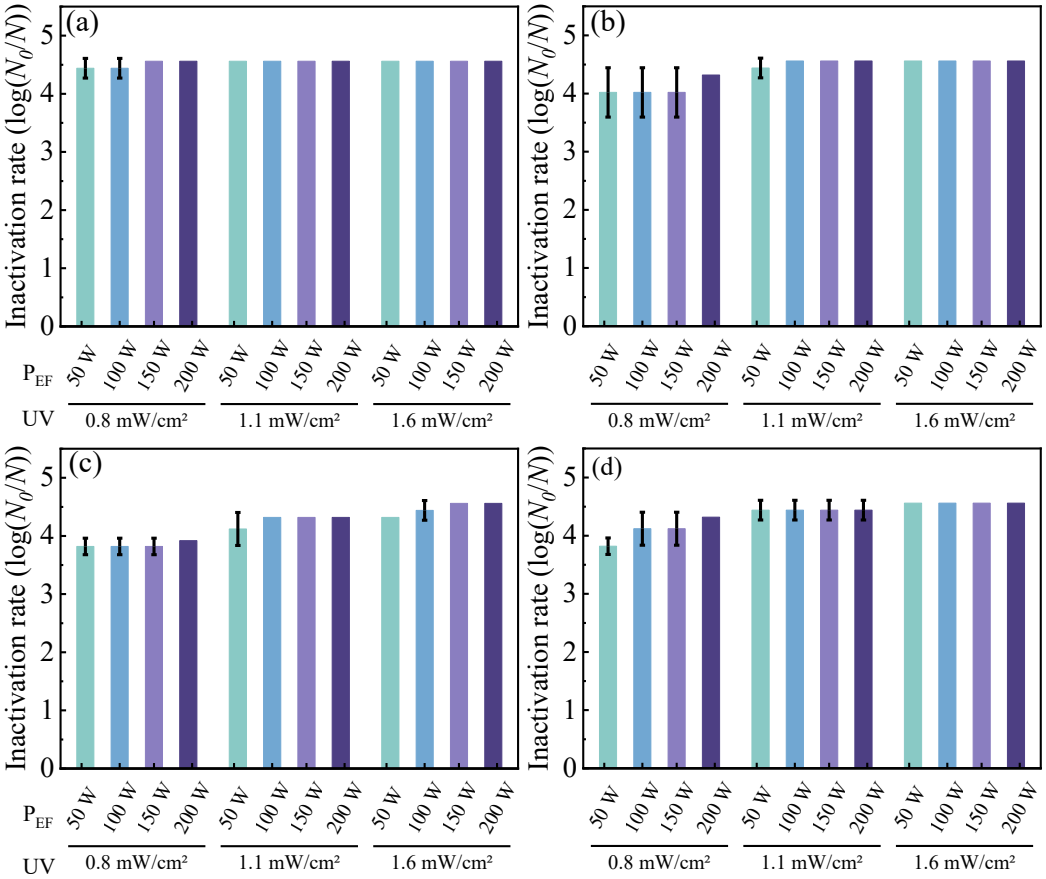


**Figure S3 The synergistic disinfection effect of *B. subtilis* by microwave-excited strong electric field and UV light:** (a) Flow rate at 50 mL/min; (b) Flow rate at 100 mL/min; (c) Flow rate at 150 mL/min; (d) Flow rate at 200 mL/min.

$P_{EF}$: Microwave-excited electric field power

*UV*: Ultraviolet intensity

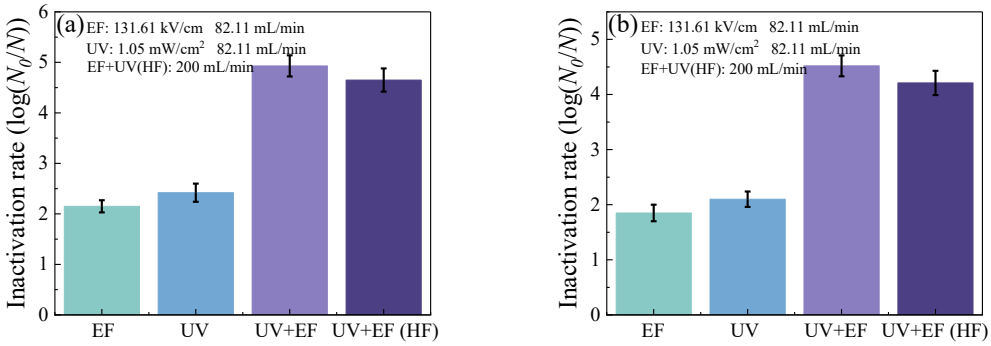


**Figure S4 The actual disinfection effect under the response surface optimization parameters:** (a) The actual effect on *E. coli*; (b) The actual effect on *B. subtilis*. (HF: High Flow Rate)

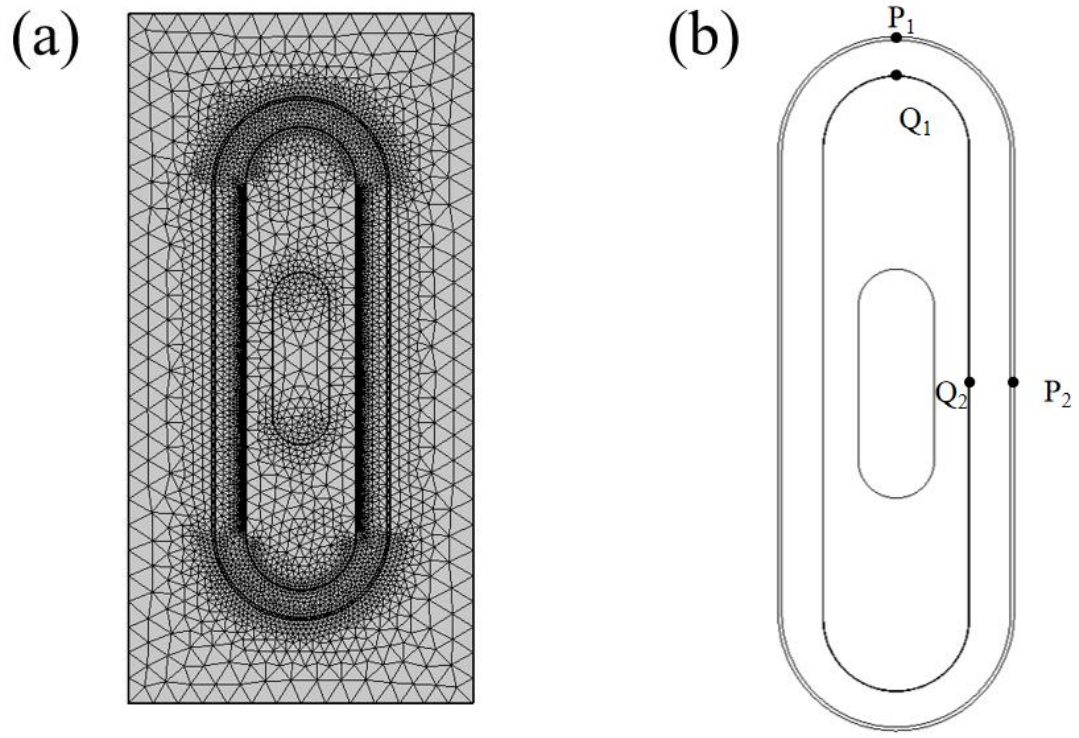


**Figure S5 Schematic diagram of grid division of the *Escherichia coli* simulation model**

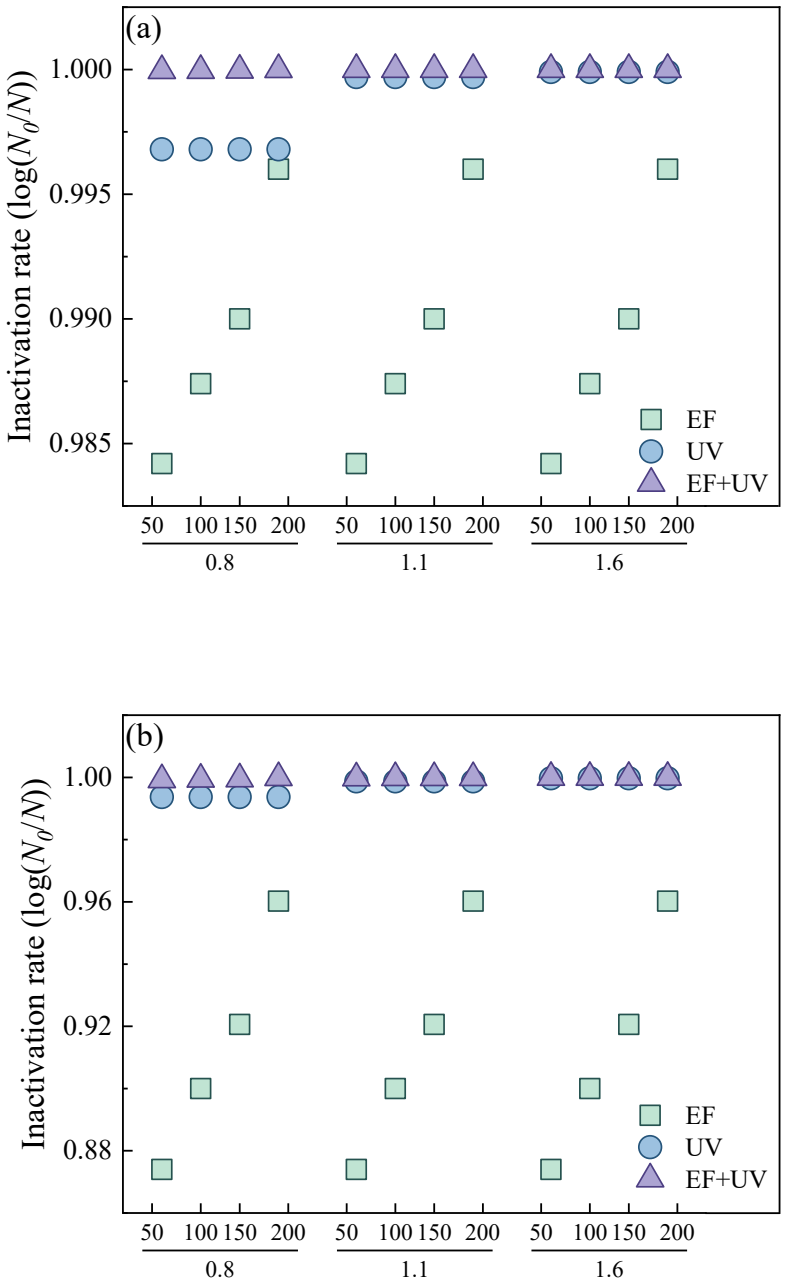


**Figure S6 The cumulative prediction curve of the synergistic disinfection theory of microwave synchronous excitation electric field and ultraviolet radiation:** (a) The effect on *E. coli*; (b) The effect on *B. subtilis*.

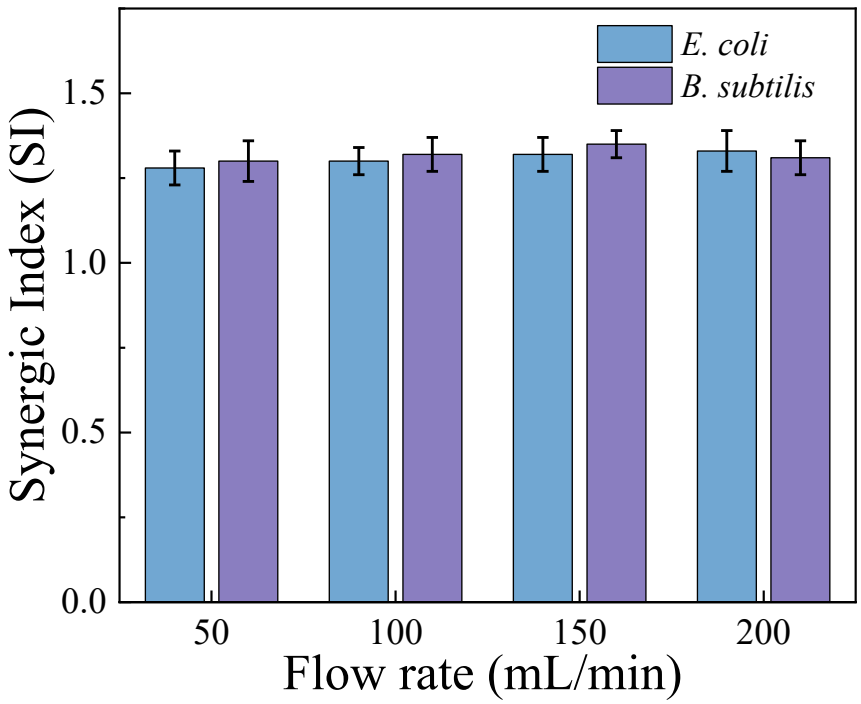


**Figure S7 The synergy index under non-saturated conditions (ultraviolet radiation 0.8 mW/cm²).**

**Table S1 Parameters related to the *E.coli* electroporation model**

| Parameters | Physical quantities | Parameter values |
|---|---|---|
| Geometric parameters /(m) | Cell length | $2\times10^{-6}$ |
| | Cell radius | $5\times10^{-7}$ |
| | Cell wall thickness | $2.4\times10^{-8}$ |
| | Cell membrane thickness | $5\times10^{-9}$ |
| | Extracellular radius of the cytoplasm | $9.52\times10^{-7}$ |
| | Nucleoid radius | $2.5\times10^{-7}$ |
| Conductivity /($S\cdot m^{-1}$) | Extracellular fluid conductivity | 0.1 |
| | Cell wall conductivity | $3.9\times10^{-5}$ |
| | Periplasmic conductivity | 0.4 |
| | Cell membrane conductivity | $4\times10^{-7}$ |
| | Cytoplasmic conductivity | 0.22 |
| | Nucleoid conductivity | 1.35 |
| Relative dielectric constant | Extracellular fluid | 40 |
| | Cell wall | 28 |
| | Periplasmic | 60 |
| | Cell membrane | 14 |
| | Cytoplasm | 67 |
| | Nucleoid | 52 |
| Electroporation parameters | Perforation coefficient /$m^{-2}\cdot S^{-1}$ | $6\times10^{8}$ |
| | Average pore density /$m^{-2}$ | $1.5\times10^{9}$ |
| | Characteristic voltage /V | 0.17 |
| | Electroporation constant | 2.46 |
| | Micropore radius$r_p$/nm | 0.8 |
| | Micropore hindrance energy coefficient /$W_0$ | 2.65 |
| | Micropore conductivity /$S\cdot m^{-1}$ | 0.22 |
| | Relative density of micropores | 0.15 |
| | Faraday constant /()$C\cdot mol^{-1}$ | $9.65\times10^{4}$ |
| | Gas constants /$J\cdot K^{-1}\cdot mol^{-1}$ | 8.314 |
| | Absolute temperature /K | 295 |

**Table S2 Ultraviolet doses corresponding to different ultraviolet intensities**

| Flow Rate (mL/min) | Residence Time t (s) | UV Intensity (mW/cm²) | UV Dose (mJ/cm²) |
|---|---|---|---|
| | 1.2 | 0.8 | 0.96 |
| 50 | 1.2 | 1.1 | 1.32 |
| | 1.2 | 1.6 | 1.92 |
| | 0.6 | 0.8 | 0.48 |
| 100 | 0.6 | 1.1 | 0.66 |
| | 0.6 | 1.6 | 0.96 |
| | 0.4 | 0.8 | 0.32 |
| 150 | 0.4 | 1.1 | 0.44 |
| | 0.4 | 1.6 | 0.64 |
| | 0.3 | 0.8 | 0.24 |
| 200 | 0.3 | 1.1 | 0.33 |
| | 0.3 | 1.6 | 0.48 |

**References**


Guo, F., Qian, K., Li, X., & Deng, H. (2022). Simulation study of cell transmembrane potential and electroporation induced by time-varying magnetic fields. *Innovative Food Science & Emerging Technologies*, *81*. https://doi.org/10.1016/j.ifset.2022.103117

Guo, F., Yuan, H., & Dan, G. (2026). Simulation study of Escherichia coli electroporation induced by pulsed magnetic field. *Journal of Food Engineering*, *413*, 113013. https://doi.org/https://doi.org/10.1016/j.jfoodeng.2026.113013

Hijnen, W. A. M., Beerendonk, E. F., & Medema, G. J. (2006). Inactivation credit of UV radiation for viruses, bacteria and protozoan (oo)cysts in water: A review. *Water Research*, *40*(1), 3–22. https://doi.org/10.1016/j.watres.2005.10.030

Kashimada, K., Kamiko, N., Yamamoto, K., & Ohgaki, S. (1996). Assessment of photoreactivation following ultraviolet light disinfection. *Water Science and Technology*, *33*(10-11), 261–269. https://doi.org/10.2166/wst.1996.0683

Li, G.-Q., Wang, W.-L., Huo, Z.-Y., Lu, Y., & Hu, H.-Y. (2017). Comparison of UV-LED and low pressure UV for water disinfection: Photoreactivation and dark repair of Escherichia coli. *Water Research*, *126*, 134–143. https://doi.org/10.1016/j.watres.2017.09.030

Lindenauer, K. G., & Darby, J. L. (1994). Ultraviolet disinfection of wastewater: effect of dose on subsequent photoreactivation. *Water Research*, *28*(4), 805–817.

Nebot Sanz, E., Salcedo Dávila, I., Andrade Balao, J. A., & Quiroga Alonso, J. M. (2007). Modelling of reactivation after UV disinfection: Effect of UV-C dose on subsequent photoreactivation and dark repair. *Water Research*, *41*(14), 3141–3151. https://doi.org/10.1016/j.watres.2007.04.008

Pezeshkpour, V., Khosravani, S. A., Ghaedi, M., Dashtian, K., Zare, F., Sharifi, A., Jannesar, R., & Zoladl, M. (2018). Ultrasound assisted extraction of phenolic acids from broccoli vegetable and using sonochemistry for preparation of MOF-5 nanocubes: Comparative study based on micro-dilution broth and plate count method for synergism antibacterial effect. *Ultrasonics Sonochemistry*, *40*, 1031–1038. https://doi.org/10.1016/j.ultsonch.2017.09.001

Wang, T., Chen, H., Yu, C., & Xie, X. (2019). Rapid determination of the electroporation threshold for bacteria inactivation using a lab-on-a-chip platform. *Environment International*, *132*. https://doi.org/10.1016/j.envint.2019.105040